Accepted Manuscript

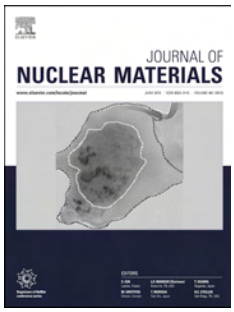

Microstructure investigations of U_3Si_2 implanted by high-energy Xe ions at 600°C

Yinbin Miao, Jason Harp, Kun Mo, Yeon Soo Kim, Shaofei Zhu, Abdellatif M. Yacout

PII: S0022-3115(17)31643-4

DOI: 10.1016/j.jnucmat.2018.02.031

Reference: NUMA 50804

To appear in: *Journal of Nuclear Materials*

Received Date: 25 November 2017

Revised Date: 23 January 2018

Accepted Date: 20 February 2018

Please cite this article as: Y. Miao, J. Harp, K. Mo, Y.S. Kim, S. Zhu, A.M. Yacout, Microstructure investigations of U_3Si_2 implanted by high-energy Xe ions at 600°C, *Journal of Nuclear Materials* (2018), doi: 10.1016/j.jnucmat.2018.02.031.

Microstructure Investigations of U_3Si_2 Implanted by High-Energy Xe Ions at 600°C

Yinbin Miao[a,*], Jason Harp[b], Kun Mo[a], Yeon Soo Kim[a], Shaofei Zhu[a], Abdellatif M. Yacout[a]

[a]*Argonne National Laboratory, Argonne, IL 60439, United States*
[b]*Idaho National Laboratory, Idaho Falls, ID 83415, United States*

Abstract

The microstructure investigations on a high-energy Xe-implanted U_3Si_2 pellet were performed. The promising accident tolerant fuel (ATF) candidate, U_3Si_2, was irradiated by 84 MeV Xe ions at 600°C at Argonne Tandem Linac Accelerator System (ATLAS). The characterizations of the Xe implanted sample were conducted using advanced transmission electron microscopy (TEM) techniques. An oxidation layer was observed on the sample surface after irradiation under the $\sim 10^{-5}$ Pa vacuum. The study on the oxidation layer not only unveils the readily oxidation behavior of U_3Si_2 under high-temperature irradiation conditions, but also develops an understanding of its oxidation mechanism. Intragranular Xe bubbles with bimodal size distribution were observed within the Xe deposition region of the sample induced by 84 MeV Xe ion implantation. At the irradiation temperature of 600 °C, the gaseous swelling strain contributed by intragranular bubbles was found to be insignificant, indicating an acceptable fission gas behavior of U_3Si_2 as a light water reactor (LWR) fuel operating at such a temperature.

Keywords: U_3Si_2, fission gas behavior, ion irradiation, light water reactor (LWR), microstructure characterization, accident tolerant fuel

1. Introduction

The East Japan Great Earthquake and Tsunami and the subsequent nuclear accident in Fukushima Daiichi Nuclear Power Plant motivated global efforts in searching for novel fuel-cladding solutions

*Tel: +1 (630)252-7448. Email: ymiao@anl.gov (Y. Miao)

with enhanced accident tolerance that can take the place of the current UO_2-zirconium alloy combination in light water reactors (LWRs) [1, 2]. The target accident tolerant fuel (ATF) materials must transcend the current UO_2 fuel in at least two aspects: thermophysical properties and uranium density. Improved thermophysical properties are expected to reduce the thermal energy stored in fuels under normal operation conditions and facilitate fuel performance for some accidents [3]. The neutronic benefits provided by a higher uranium density allow selection of cladding materials with higher neutron capture cross sections such as FeCrAl alloys [4]. Also, a high uranium density may help increase utilities' profits by extending the lifetime of fuel elements so as to promote the transition from conventional fuels to ATFs. As an intermetallic, U_3Si_2 has a higher thermal conductivity that increases with temperature [5] as well as a higher uranium density compared to UO_2. Therefore, being regarded as a promising ATF candidate, U_3Si_2 has been intensely studied in the past few years [5, 6, 7, 8, 9, 10, 11, 12, 13, 14, 15, 16].

Considering its successful applications in replacing high-enrichment low-density nuclear fuels in research reactors, which has been supported by the Reduced Enrichment for Research and Test Reactors (RERTR) program, U_3Si_2 is not an unfamiliar uranium compound to the nuclear material community [17, 18, 19, 20, 21, 22]. However, in LWRs, the operation conditions of fuels differ substantially from those in research reactors. To be specific, the fuel temperature in LWRs generally exceeds 300°C, whereas fuels in research reactors usually operate under 250°C. Therefore, despite that a great amount of U_3Si_2's in-pile irradiation experimental data are available, little is related to fuel performance under LWR conditions. Within the typical range of fuel temperature in research reactors, U_3Si_2 suffers radiation-induced amorphization with a dose threshold of merely 0.3 dpa [23]. Thus, during the vast majority of the operating time in research reactors, U_3Si_2 exists in its amorphous phase. However, as temperature is beyond approximately 250°C, which is the case in LWRs, U_3Si_2 seems to be immune to amorphization under irradiation [11, 13, 15]. The fuel behavior of U_3Si_2 under LWR conditions can differ dramatically from what was observed in research reactors due to the fundamental difference in atomic structure at different temperatures. Hence, experimental data collected from research reactor experiments alone cannot provide sufficient references to evaluate U_3Si_2's fuel performance in LWRs.

Originating from the accumulation of gaseous fission products in nuclear fuels, fission gas behavior leads to a series of issues that degrade fuel performance and may compromise fuel integrity, such as gaseous swelling, fission gas release, and thermal conductivity reduction. Consequently, fission gas behavior of U_3Si_2 in LWRs must be comprehensively understood and then accurately predicted, in order to qualify this uranium compound as a LWR fuel material with enhanced accident tolerance. However, the development of advanced fuel performance models requires experimental data of radiation-induced fuel modifications at LWR temperatures for verification and validation. Recently, the radiography investigation of the in-pile-irradiated U_3Si_2 (as a part of the ATF-1 irradiation campaign) unveiled that U_3Si_2 pellets are largely intact and free from run-away swelling at ~6×10^{20} fissions/cm^3 [24]. This encouraging progress provides important qualitative observations of in-pile fuel performance of U_3Si_2 in LWRs, whereas detailed microstructure information of the fission gas behavior in those pellets will not be available to the ATF community for a while considering the high financial cost and technical challenges involved in the PIE efforts of in-pile-irradiated fuels. Meanwhile, heavy ions with ~1 MeV per nucleon has recently been proved to be capable of replicating a series of radiation-induced microstructural modifications in nuclear fuel materials by simulating the fission products with ~100 MeV kinetic energy [25, 26, 27, 28, 29]. Thus, it is of great relevance to adopt high-energy heavy ion irradiation and corresponding PIE techniques, as an economical and efficient tool that is complementary to in-pile irradiation tests, to produce experimental data to support fuel performance model development of U_3Si_2 under LWR conditions. In this regard, Xe, the most representative gaseous fission product, was ionized, accelerated, and implanted into U_3Si_2 samples at LWR temperatures by Argonne Tandem Linac Accelerator System (ATLAS). At 300°C, small lattice intragranular bubbles with monomodal size distribution were observed along with small bubbles aggregated on defect sinks such as dislocations and grain boundaries [13]. As temperature increases, some bubble evolution kinetics with higher energy barriers may be activated, resulting into a dissimilar bubble morphology [12]. In this study, the microstructural modifications, especially Xe bubble morphology, induced by Xe ions at 600°C were focused on so that additional fission gas behavior of U_3Si_2 under LWR conditions can be disclosed.

2. Experiments

2.1. Sample Preparation

The U_3Si_2 cylindrical pellet with an 8.3 mm diameter investigated in this study was fabricated at Idaho National Laboratory [8] using the same procedures and conditions as those pellets irradiated in the Advanced Test Reactor (ATR) for the ATF-1 campaign [7]. The fine depleted uranium powder (92.5 wt%) was mixed and pressed at 225 MPa with fine silicon powder (7.5 wt%) before being arc-melted to form U_3Si_2 ingots. A fine powder of U_3Si_2 was produced by comminuting those ingots and was then used to fabricate U_3Si_2 pellets by cold pressing and sintering in an argon protection atmosphere. More details about the fuel fabrication procedures can be found in Ref. [8]. The manufacturers have reported the existence of USi and UO_2 precipitates (~14 vol.%) in the as-fabricated U_3Si_2 pellets. U-Si phases with higher U content, such as U_3Si and U(Si), were not observed. A 3 mm thick disk was cut from the pellet using a diamond saw for the high-energy Xe implantation. The surface subject to ion irradiation was first mechanically polished to 0.05 μm surface roughness and then vibratory polished to its final surface finish.

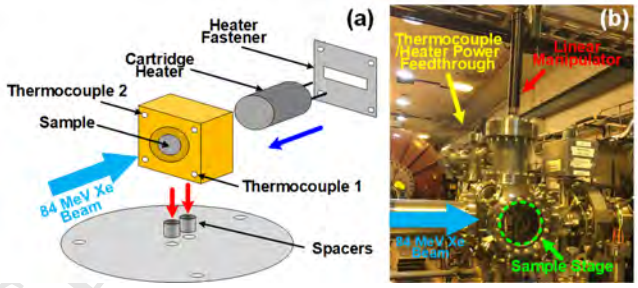

Figure 1: Experiment setup of Xe implantation at ATLAS: (a) a schematic showing the design of the irradiation sample stage; (b) the irradiation sample stage installed between the Boost linac and PII linac of the ATLAS facility.

2.2. Ion Implantation

The high-energy Xe implantation was conducted at the ATLAS ion irradiation chamber, which is capable of accelerating a wide range of species of ions (from proton to uranium) up to ~1.5 MeV per nucleon [27]. The U_3Si_2 disks was fastened to a sample holder made

of oxygen-free high-conductivity (OFHC) copper using PELCO high performance silver paste. Also mounted on the OFHC copper sample holder was a HeatWave Labs TB-175 cartridge heater. The heater used a tunable DC power supply controlled by a proportional-integral-derivative (PID) module. The temperature of the specimen was measured by two K-type thermocouples mounted ~5 mm away from the specimen (Fig. 1). The specimen was heated to 600°C at a 60°C/min ramping rate and then irradiated by 84 MeV Xe ions of ~100 particle nA. The irradiation temperature was within the typical LWR fuel temperature range but was much higher than the typical fuel surface temperature (~300°C), as investigated previously [13]. Throughout the Xe implantation, the temperature fluctuation was limited by the PID within ±10°C. The temperature difference between the sample surface and thermocouple positions was found to be lower than 20°C when a heater working at 200 W was attached to the sample surface to simulate irradiation heating effect. Considering that the ion beam used in this study had a power of merely 8.4 W, the measured temperature only has a marginal difference from the actual irradiation temperature. The energy of Xe ions was similar to that of the Xe fission fragments in actual in-pile irradiated fuels and therefore was expected to simulate the radiation-induced microstructural modifications. The profile of the Xe ion beam was measured and centered by a Faraday cup. The U_3Si_2 specimen was continuously irradiated at a 100 particle nA beam current for 20 hours. Assuming a 2D Gaussian beam profile, the ion fluence in the center of the beam's footprint was determined to be 1.38×10^{17} ions/cm^2. The Xe deposition and radiation dose profiles induced by this fluence of Xe ions were assessed using the quick damage mode of SRIM code [30] and Stoller et al.'s approach [31] (E_d^U = 61 eV [32, 33]; E_d^{Si} = 15 eV), as shown in Fig. 2(b). The peak radiation dose (499 dpa) appears at approximately 6 μm from the surface, whereas the average Xe concentration from 5 μm to 8 μm from the surface is approximately 0.92%, which is equivalent to a approximately 6.4%FIMA (fissions per initial metal atom) assuming a gas fission product yield of 0.24 [34].

2.3. Characterization of the Irradiated Specimen

The microstructure characterization of the Xe-implanted U_3Si_2 sample was performed at the Materials Characterization Suite (MaCS) in Center for Advanced Energy Studies (CAES). A transmission electron microscopy (TEM) lamella specimen was lifted out from the center of

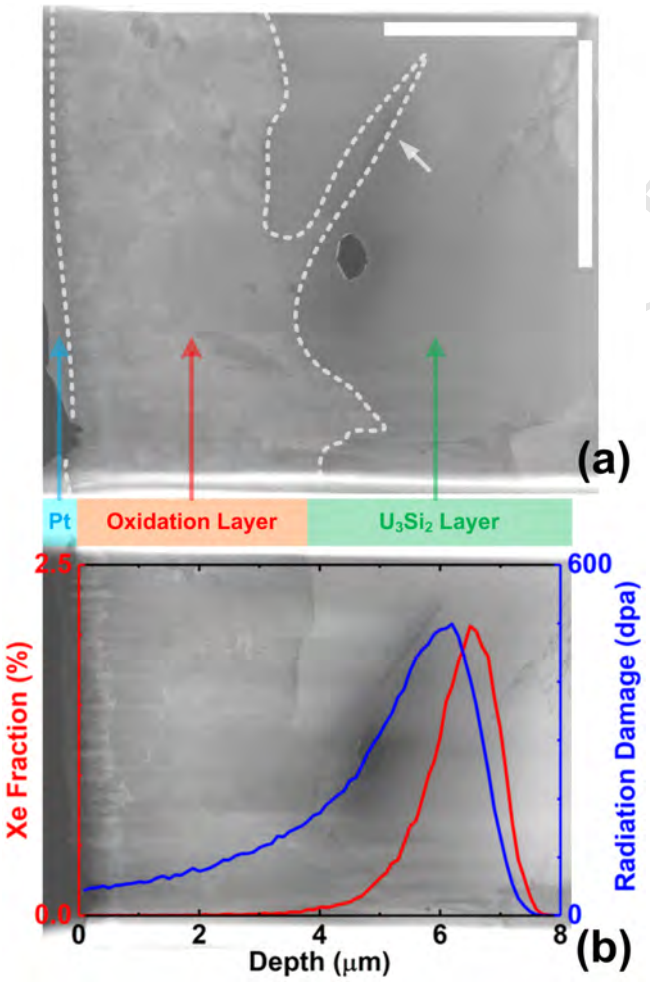

Figure 2: Overview of the investigated TEM lamella: (a) a SEM secondary electron image of the TEM specimen during FIB preparation, showing the multilayer structure (including Pt protection layer, oxidation layer (OL), and U_3Si_2 layer) in the depth direction. The white arrow marks an oxidized area in the U_3Si_2 layer that used to be a grain boundary. The bright and dark features around 8 μm deep in the specimen are UO_2 and USi precipitates forming during the sintering of the U_3Si_2 pellets. Both of the scale bars indicate a length of 3 μm in their respective directions. (b) a STEM HAADF Z-contrast image of the TEM specimen showing the layer division in the depth direction, overlaid with the Xe concentration and radiation damage profiles calculated by SRIM. It is worth mentioning that a small portion of the OL layer near the surface was intentionally not processed by the Ga ion beam during the final thinning in FIB so as to preserve the Pt protection layer as the surface reference. As a result, that small portion of the OL near the surface shows brighter contrast due to the extra thickness.

the ion beam's footprint on the U_3Si_2 sample and mounted onto a copper Omniprobe TEM grid in an FEI Quanta 3D FEG focused ion beam (FIB) system. An approximately 6 μm (width) $\times$ 10 μm (depth) rectangular area on the lamella was then further thinned to electron transparency (approximately 50 nm) by the FIB. The completed TEM lamella was investigated using an FEI Tecnai TF30-FEG STwin STEM working at 300 kV. A series of imaging techniques, such as TEM bright-field (BF) diffraction contrast imaging and scanning transmission electron microscopy (STEM) high-angle annular dark field (HAADF) Z-contrast imaging, were employed to explore the radiation-induced microstructural modifications, bubble morphology in particular, in the Xe implanted U_3Si_2 specimen. In addition, analytic STEM techniques such as energy dispersive X-ray spectroscopy (EDS or EDX) were adopted to characterize the element composition of different phases observed in the lamella.

3. Results

3.1. The Oxidation Layer and Si-Enriched Layer

One of the most prominent microstructural modifications observed in the lamella is the formation of the oxidation layer (OL). U_3Si_2 has been reported to be subject to radiation-enhance or radiation-induced oxidation even under vacuum (on the order of 10^{-5} or 10^{-6} Pa) [35, 11, 13]. In a previous study on U_3Si_2 irradiated at 300°C [13], an approximately 1 μm thick OL mainly comprising nanocrystalline UO_2 was reported to form on the surface exposed to irradiation. In this study, as the irradiation temperature was increased by 300°C, the thickness of the OL was quadrupled due to the fast diffusion at elevated temperatures (Fig. 2). A close look into the OL (Fig. 3(a)) shows the similar nanocrystalline structure as reported in U_3Si_2 irradiated at 300°C [13]. The selected area diffraction pattern (SADP) of the OL zone (Fig. 3(b)) indicates that the vast majority of the diffraction spots comes from UO_2 nano-grains (red rings), and that a small fraction of diffraction spots may be probably contributed by other U-O or U-Si compounds such as U_3O_8, U_3Si_2, U_3Si, and USi. The STEM HAADF Z-contrast image of the OL zone (Fig. 3(c) and (d)) also illustrates some high-Z and low-Z precipitates embedded in the OL matrix. Compared to the EDS profile of the U_3Si_2 (Fig. 3(e)), the EDS profile of the OL matrix (Fig.

3(f)) shows the absence of Si and enrichment of O, which is consistent with the dominant UO_2 diffraction contribution in the OL. In TEM and STEM images, the OL seems free of cracks and cavities. Thus, the OL is dense and expected to be protective. On the other hand, according to EDS(Fig. 3(g) and (f)), the high-Z precipitates were found to be U-enriched and Si-depleted, whereas the low-Z precipitates are U-depleted and Si-enriched. This finding explains those minor diffraction spots, and thus implies the occurrence of phase decomposition in the OL zone.

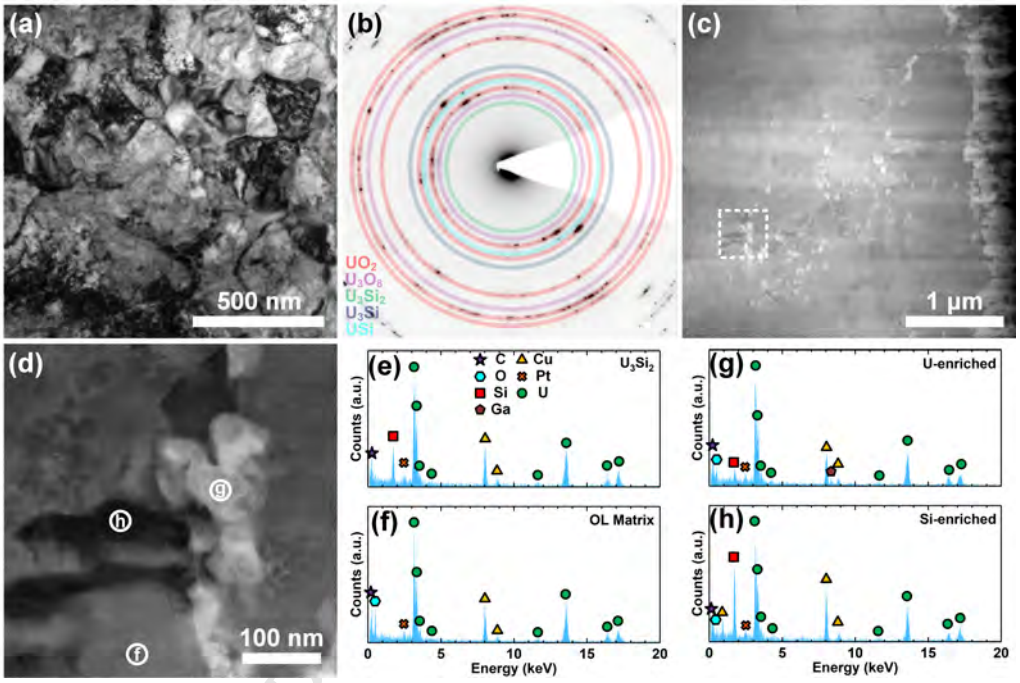

Figure 3: Microstructure of the oxidation layer (OL): (a) a TEM BF image of the OL showing the diffraction contrast of nano-grains; (b) the selected area diffraction pattern (SADP) of the OL showing the dominance of the nanocrystalline UO_2 phase and co-existing minor phases such as U_3O_8, U_3Si_2, USi, and residual U_3Si_2; (c) a STEM HAADF Z-contrast image of the OL indicating the existence of minor phases with different compositions; (d) the magnified STEM HAADF Z-contrast image of the area indicated by the white frame in (c), showing the low-Z (darker, labeled by "h"), high-Z (brighter, labeled by "g"), and medium-Z matrix (labeled by "f") zones; (e) the EDS data of the U_3Si_2 taken at the U_3Si_2 layer in Fig. 2; (f) the EDS data of the medium-Z matrix zone labeled by "f" in (d), showing the absence of Si and enrichment of O compared to U_3Si_2; (g) the EDS data of the high-Z zone labeled by "g" in (d), showing the depletion of Si compared to U_3Si_2; (h) the EDS data of the low-Z zone labeled by "h" in (d), showing the enrichment of Si compared to U_3Si_2.

In the U_3Si_2 irradiated at 300°C, Si was found to diffuse away from the surface, leaving a Si-depleted OL zone and forming a ~50 nm thick Si-enriched layer (SEL) between the OL and U_3Si_2 [13]. Similar phenomenon was observed in this study as the irradiation temperature was

increased to 600°C. In STEM HAADF Z-contrast images (Fig. 2(b) and Fig. 4(a)), a low-Z layer can be distinguished between the OL and U_3Si_2. EDS profile of this low-Z layer (Fig. 4(c)) confirms that this is the SEL. As the OL zone was thickened fourfold at the higher irradiation temperature, the SEL also increased in thickness. The thicker SEL made it possible to obtain its diffraction pattern. As shown in Fig. 4(b), the SEL was determined to be USi_{2-x} [36]. It is worth mentioning that some forbidden diffraction spots of USi_{2-x} are also present, implying the high concentration of radiation-induced point defects and/or anti-site defects in this zone.

Figure 4: Microstructure of the Si-enriched layer (SEL): (a) a STEM HAADF Z-contrast image showing the formation of a low-Z layer between the OL and the U_3Si_2 layers; (b) the SADP of the SEL zone that was identified as the (010) zone of USi_{2-x}; the forbidden diffraction spots that appear in this SADP are labeled by orange indices; (c) the EDS data of the SEL zone, showing the enrichment of Si compared to U_3Si_2 (Fig. 3(e)).

3.2. The Bubble Region

Beyond the SEL zone is the U_3Si_2 zone confirmed by both the EDS profile (Fig. 3(e)) and SADP (Fig. 5(b) and (c)). Similar to the SADP of the SEL, some forbidden diffraction spots of U_3Si_2, such as the {100} spots, are present, indicating the high density of radiation-induced defects in this region. Additionally, a blade-shaped feature with a thickness of approximately 300 nm from the OL and SEL zones extended into the U_3Si_2 zone (marked by the white arrow in Fig. 2), dividing this zone into two parts labeled G1 and G2, respectively (Fig. 5(a)). The SADPs of those two parts (Fig. 5(b) and (c)) indicate that they are two U_3Si_2 grains with a misorientation of approximately 2.7°. Thus, the blade-shaped feature used to be a low-angle grain boundary (LAGB) prior to the Xe implantation. According to the SRIM calculation, both

Xe concentration and radiation dose profiles peak in the region shown in Fig. 5(a). This region can then be termed as the bubble region because Xe bubbles are expected to form in it. The bubble region is still dominated by U_3Si_2 phase though the area surrounding the LAGB was oxidized during irradiation. Hence, the bubble morphology investigations in this study were still feasible in spite of the surface oxidation issue. It is worth mentioning that a small amount of oxygen that is lower than the detection limit of STEM EDS technique (Fig. 3(e)) may diffuse into the U_3Si_2 layer, affecting the local defect kinetics.

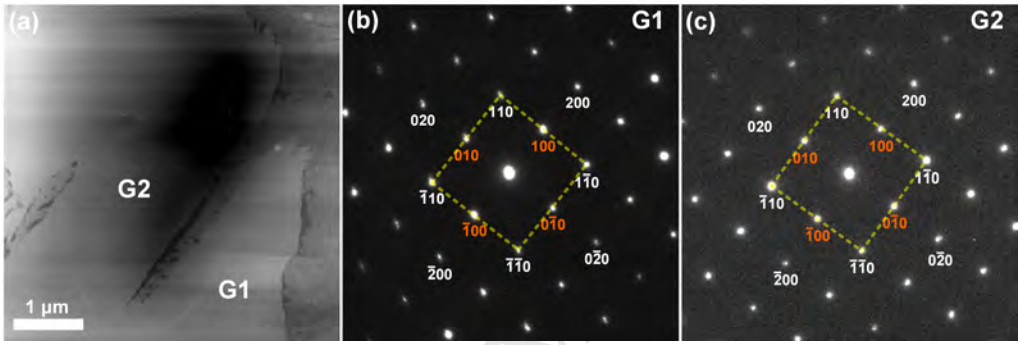

Figure 5: Microstructure of the U_3Si_2 zone where Xe concentration and radiation damage profiles peak: (a) a STEM HAADF Z-contrast image of the U_3Si_2 bubble region; (b)(c) the SADPs of the two regions labeled by G1 and G2 in (a), showing a slight misorientation of approximately 2.7°; the forbidden diffraction spots that appear in these SADPs are labeled by orange indices.

3.3. Bubble Morphology

In the bubble region of the investigated TEM lamella, as the only grain boundary was preferentially oxidized during the Xe implantation, the bubble morphology investigations in this study were focused on intragranular bubbles. Near the peak of the Xe concentration profile, the most prominent microstructure feature is the bubbles of approximately 20 nm in diameter. This feature can be recognized in both STEM HAADF Z-contrast images (Fig. 6(a)) and defocused TEM BF diffraction contrast images (Fig. 6(b)). Those intragranular bubbles with sizes on the order of 10 nm usually have a faceting rather than spherical shape (Fig. 6(c)). The number density and size distribution of those bubbles near the Xe concentration peak were obtained by analyzing images of over 100 bubbles using both imaging techniques. The STEM HAADF Z-contrast

images give a bubble number density of 8.6×10^{20} m^{-3} and an average size of 23.6±0.9 nm (Fig. 6(a)), whereas the 1 μm overfocused TEM BF images yields a number density of 8.5×10^{20} m^{-3} and an average size of 22.2±1.0 nm (Fig. 6(b)). The two imaging techniques produce consistent statistics of bubble morphology considering the margins of error.

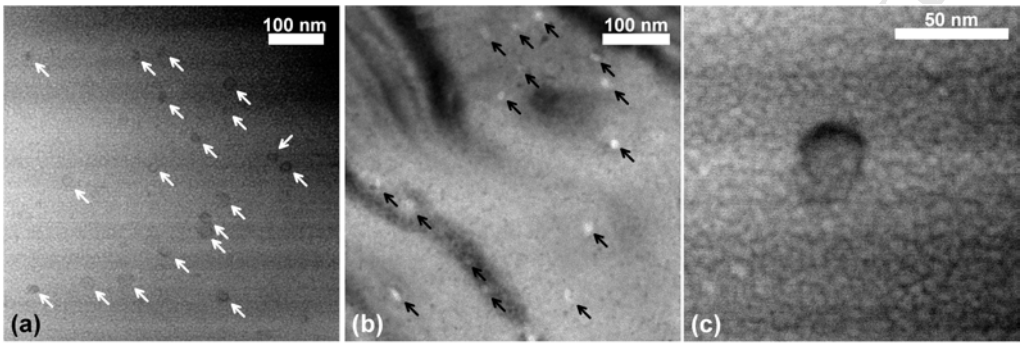

Figure 6: Morphology of large intragranular bubbles (indicated by black and white arrows): (a) a STEM HAADF image of the U_3Si_2 region near the Xe concentration peak showing the existence of intragranular Xe bubbles of the order of 10 nm; (b) a 1 μm overfocused TEM BF image of the U_3Si_2 region near the Xe concentration peak showing the existence of intragranular Xe bubbles of the order of 10 nm; (c) a magnified STEM HAADF image showing a faceted intragranular bubble of 34.7 nm in diameter.

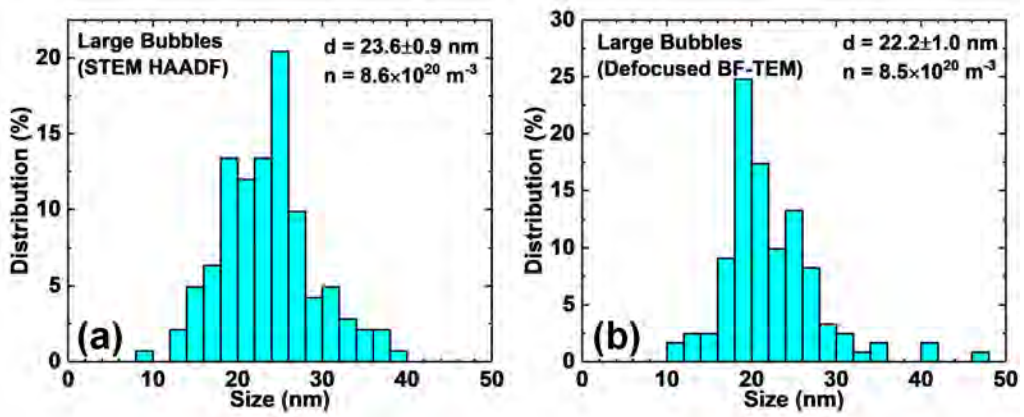

Figure 7: Size distribution of large intragranular bubbles: (a) size distribution of large intragranular bubbles measured from the STEM HAADF Z-contrast images; (b) size distribution of large intragranular bubbles measured from 1 μm overfocused TEM BF images.

Aside from those bubbles of tens of nm, smaller intragranular bubbles also form in the bubble region. Due to the limited size, those small bubbles cannot be resolved in STEM HAADF

images. However, TEM BF defocused imaging is still capable of visualizing them. Even in the low-magnification overfocused image such as Fig. 6(b), small dark spots can be distinguished along with those aforementioned large bubbles. In higher magnification, those small intragranular bubbles with sizes on the order of several nm can be recognized as white and black spherical spots in underfocused and overfocused images, respectively (Fig. 8).

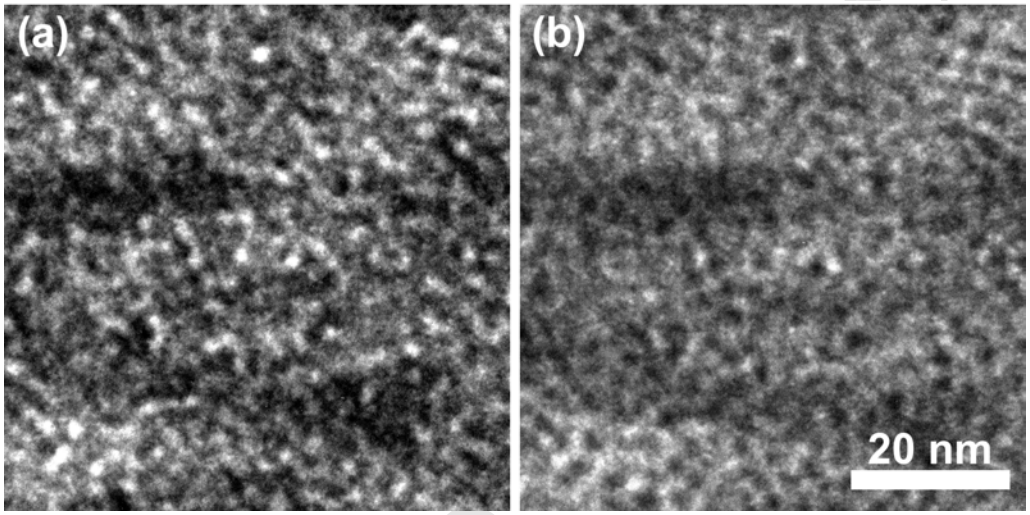

Figure 8: Morphology of small intragranular bubbles: (a) a 1 μm underfocused TEM BF image of the U_3Si_2 region near the Xe concentration peak showing the intragranular Xe bubbles (brighter spots) on the order of 1 nm; (b) a 1 μm overfocused TEM BF image showing the same intragranular bubbles as dark spots.

The number density of those small intragranular bubbles exceeds that of the large intragranular bubbles by approximately three orders of magnitude. In additions, the average size of the small intragranular bubbles was found to be 2.87±0.07 nm with a distribution ranging from 1.8 nm to 4 nm, as shown in Fig. 9. Therefore, the intragranular bubbles in the Xe implanted U_3Si_2 specimen show a bimodal size distribution, as shown in Figs. 7 and 9 respectively.

4. Discussion

4.1. Oxidation Mechanism

Microstructure studies on corrosion issues have been performed recently for U_3Si_2 and its non-radioactive surrogate with and without irradiation [37, 38, 11, 13, 39, 40]. When no irradiation

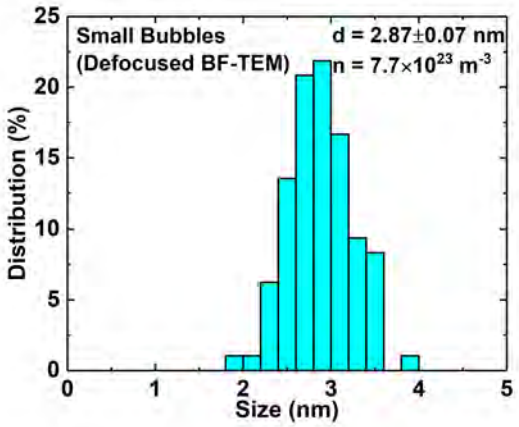

Figure 9: Size distribution of small intragranular bubbles measured from 1 μm overfocused TEM BF images.

was involved, the onset of reaction with steam was reported to occur at approximately 400°C to 500°C [40, 38]. In high-temperature corrosion tests of U_3Si_2 in air, the oxidation products were reported to be UO_2, U_3O_8, and USi_3 [40]. Under irradiation, U_3Si_2 was found to oxidize even under high-vacuum conditions in TEM [11, 15] and accelerator chambers even at 300°C [13], which is lower than the onset temperature without irradiation. Thus, the oxidation behavior of U_3Si_2 is obviously facilitated by irradiation. The product of oxidation is either nanocrystalline UO_2 plus amorphous SiO_2 in *in situ* TEM ion irradiation [11], or a layer of UO_2 nano-grains plus a layer of Si-enriched phase in a bulk sample irradiated at 300°C [13]. In this study, with the increase of irradiation temperature, oxidation impacted a thicker region of the U_3Si_2, which helps unveil more microstructure information of the oxidation mechanism in irradiated U_3Si_2.

First of all, the OL is mainly composed of nanocrystalline UO_2, which is consistent with the observation at 300°C [13]. As the thickness of the OL was quadrupled due to the elevated temperature, more details in microstructure of the OL can be discovered. Aside from a limited amount of residual U_3Si_2, the existence of a U-enriched phase (U_3Si) and a Si-enriched phase (USi) can be confirmed by both crystal structure and element composition characterizations, indicating the occurrence of phase decomposition. This decomposition may be related to the

depletion of Si in the OL. Electron diffraction also indicated the formation of U_3O_8 in addition to UO_2, probably due to the increase of irradiation temperature.

Also in agreement with the previous study at 300°C [13] is the formation of a SEL between the OL and U_3Si_2. At 600°C, accompanied with the increased thickness of the OL, the SEL also appears to be thicker and thus provides sufficient volume for SADP to determine its USi_{2-x} structure. Therefore, a hypothetic oxidation mechanism of U_3Si_2 under irradiation can be established: the Si tends to diffuse away from the surface exposed to oxygen and irradiation, and to form a USi_{2-x} layer, leaving the U to be oxidized into nanocrystalline UO_2. It is still unclear whether this redistribution of Si originates from radiation-induced segregation (RIS) or temperature gradient created by ion implantation. At elevated temperatures, UO_2 can be further oxidized into U_3O_8. Meanwhile, phase decomposition of U_3Si_2 may occur during the Si diffusion procedure, leaving a small portion of residual U_3Si and USi phases along with residual U_3Si_2 phase in the OL.

Finally yet importantly, preferential oxidation of grain boundaries was also observed in this study. Although U_3Si_2 becomes readily to oxidize under irradiation. The oxidation is not expected to be a serious issue for U_3Si_2 in LWRs considering that the pellet surfaces are the only open surfaces. During normal operation, the surface temperature of U_3Si_2 pellet is low, while the residual oxygen in the helium fill gas is limited. Thus, only a thin layer of surface region (several microns) may be affected.

4.2. Fuel Stability

Beyond the surface oxidation, the underneath U_3Si_2 material remained intact during the ion irradiation up to 499 dpa dose. The tetragonal crystal structure of U_3Si_2 was preserved without any distinguishable sign of amorphization or grain subdivision, showing the phase stability of U_3Si_2 under ion irradiation at 600°C. In fact, compared to the formation of high-density radiation-induced dislocations in U_3Si_2 implanted by Xe at 300°C, the U_3Si_2 grains contain few dislocations after 499 dpa irradiation due to the annealing effect at 600°C. Thus, this study further confirmed that U_3Si_2 is capable of maintaining its crystalline phase under LWR conditions. However, heavy ion irradiation still induced significant damage into the U_3Si_2 lattice. As implied

by the appearance of forbidden diffraction spots, the U_3Si_2 phase near the radiation dose peak contains a great number of radiation-induced point defects and/or anti-site defects.

4.3. Fission Gas Behavior

The quantitative morphology information of intragranular bubbles forming at this irradiation temperature is the most crucial result of this study. Unlike the irradiation test performed at 300°C [13], few radiation-induced dislocations can be distinguished in the sample irradiated at 600°C. As a result, dislocation bubbles (bubbles nucleated at dislocations) make marginal contributions to fission gas behavior at this temperature, and almost all the intragranular bubbles are lattice bubbles. In actual LWRs, lower radiation damage rate and longer annealing time compared to accelerated ion irradiation experiments may lead to an even lower density of radiation-induced dislocations. At 300°C, the lattice bubbles feature a monomodal size distribution with an average size of 2.71±0.08 nm [13]. On the contrast, at 600°C, large intragranular bubbles also form in addition to the small intragranular bubbles of several nm in size, giving a bimodal size distribution. The formation of large intragranular bubbles indicates the occurrence of bubble coalescence [41, 42, 43]. Thus, the diffusion of small Xe bubbles, which is inactive at 300°C, was found to be activated as the irradiation temperature reaches 600°C. The transition from monomodal size distribution to bimodal size distribution of lattice intragranular bubbles from 300°C to 600°C also validates the rate theory model [44] parameterized for U_3Si_2 under LWR conditions [12]. With the appearance of the large intragranular bubble, there exist a slight decrease in number density and a slight increase in average size of small intragranular bubbles. This observation is also in agreement with the rate theory prediction [12]. More importantly, with the bubble morphology data collected in this study, the parameters of the rate theory model can be further optimized.

Trial to investigate intergranular bubbles was made by preparing another TEM lamella using FIB. A high-angle grain boundary (HAGB) was observed in the bubble region of the second sample. Unfortunately, the HAGB also suffered preferential oxidation, implying that preferential oxidation of grain boundaries in the U_3Si_2 layer may be a general phenomenon at this temperature. Thus, the morphology of intergranular bubbles could not be obtained in this study. The lattice

intragranular bubbles do not exceed 50 nm (see Fig. 7) in size and contribute approximately 1.54% gaseous swelling strain in U_3Si_2 implanted to a Xe concentration equivalent to ~6.4%FIMA at 600°C, based on the size distribution and number density shown in Figs. 7 and 9. Although the swelling strain contributed by lattice bubbles is slightly higher than that of the sample irradiated at 300°C, it is still within an acceptable range, suggesting that U_3Si_2 has acceptable fission gas behavior at 600°C in regards of intragranular bubbles. It needs to be emphasized again that a higher radiation dose rate and a shorter annealing time were involved in this ion irradiation study compared to actual LWR neutron irradiation conditions, as the nature of the accelerated irradiation test utilizing high-energy heavy ions. Thus, not all the radiation-induced microstructural modifications during in-pile irradiation can be quantitatively replicated in this study. Nevertheless, as a series of important condition parameters, such as irradiation temperature, kinetic energy of the fission product (Xe), and implanted Xe concentration, were simulated to a considerable extent, this study is expected to produce reasonable results to help understand fission gas behavior of U_3Si_2 in LWRs with at least qualitative correctness. Therefore, the bubble morphology data collected in this study will help support the development of advanced fuel performance models by clarifying microstructure evolution mechanisms and providing valuable verification and validation references, especially prior to the release of the detailed PIE data from the ATF-1 in-pile irradiation campaign.

5. Conclusions

In summary, a U_3Si_2 pellet was irradiated by 84 MeV Xe ions at 600°C to simulate its fission gas behavior in LWRs. TEM/STEM characterizations disclosed a number of radiation-induced microstructural modifications. A nanocrystalline UO_2 layer along with a USi_{2-x} layer was found to form as the consequence of radiation-induced or -enhanced oxidation. The U_3Si_2 fuel was proven to maintain its crystal structure in absence of amorphization and grain subdivision up to 499 dpa at 600°C. More importantly, lattice bubbles with bimodal size distribution dominate the intragranular bubbles, whereas few dislocation bubbles were observed due to the low dislocation density at elevated temperatures. The bubble morphology data obtained in this study are complementary

to the previous study performed at a lower temperature [13]. By utilizing high-energy heavy ion irradiation and advanced microstructure characterization techniques, this study produced experimental references that are valuable for the fuel performance evaluation of U_3Si_2 as an LWR ATF.

6. Acknowledgments

This work was funded by the Accident Tolerant Fuel High-Impact Problems (ATF HIP) of the U.S. Department of Energy (DOE)'s Nuclear Energy Advanced Modeling and Simulation (NEAMS) program. The authors would also like to acknowledge the help of Matthew Hendricks on the ATLAS irradiation. This research used resources of Argonne National Laboratorys ATLAS facility, which is a DOE Office of Science User Facility. The efforts involving Argonne National Laboratory were sponsored under Contract no. DE-AC02-06CH11357 between UChicago Argonne, LLC and the U.S. Department of Energy. This work was supported by the U.S. Department of Energy, Office of Nuclear Energy under DOE Idaho Operations Office Contract DE-AC07-051D14517 as part of a Nuclear Science User Facilities experiment. The isotope(s) used in this research were supplied by the United States Department of Energy Office of Science by the Isotope Program in the Office of Nuclear Physics.

Fabrication of the samples used in this work was supported by the U.S. Department of Energy, Office of Nuclear Energy. Fabrication was part of a collaboration led by Westinghouse Electric Company comprising several national laboratories, vendors, and universities awarded in response to the DE-FOA-0001063 funding opportunity. The authors would like to acknowledge the assistance of the support staff associated with the Fuels Applied Science Building at Idaho National Laboratory specifically Rita Hoggan for preparing samples for ion irradiation.

References

[1] J. Carmack, F. Goldner, S. M. Bragg-Sitton, L. L. Snead, in: Proc. 2013 LWR Fuel Performance Meeting/TopFuel 2013, pp. 15–19.

[2] S. J. Zinkle, K. A. Terrani, J. C. Gehin, L. J. Ott, L. L. Snead, Journal of Nuclear Materials 448 (2014) 374–379.

[3] K. A. Terrani, D. Wang, L. J. Ott, R. O. Montgomery, Journal of Nuclear Materials 448 (2014) 512–519.

[4] N. M. George, K. A. Terrani, J. J. Powers, ORNL/TM-2013 121 (2013).

[5] J. White, A. Nelson, J. Dunwoody, D. Byler, D. Safarik, K. McClellan, Journal of Nuclear Materials 464 (2015) 275–280.

[6] K. Metzger, T. Knight, R. Williamson, in: Proceedings of the International Congress on Advances in Nuclear Power Plants–ICAPP 2014, Charlotte, NC.

[7] J. Carmack, K. Barrett, H. MacLean-Chichester, Light Water Reactor Accident Tolerant Fuels Irradiation Testing, Technical Report, Idaho National Laboratory (INL), Idaho Falls, ID (United States), 2015.

[8] J. M. Harp, P. A. Lessing, R. E. Hoggan, Journal of Nuclear Materials 466 (2015) 728–738.

[9] S. Middleburgh, R. Grimes, E. Lahoda, C. Stanek, D. Andersson, Journal of Nuclear Materials 482 (2016) 300–305.

[10] L. He, J. M. Harp, R. E. Hoggan, A. R. Wagner, Journal of Nuclear Materials 486 (2017) 274–282.

[11] Y. Miao, J. Harp, K. Mo, S. Bhattacharya, P. Baldo, A. M. Yacout, Journal of Nuclear Materials 484 (2017) 168–173.

[12] Y. Miao, K. A. Gamble, D. Andersson, B. Ye, Z.-G. Mei, G. Hofman, A. M. Yacout, Nuclear Engineering and Design 322 (2017) 336–344.

[13] Y. Miao, J. Harp, K. Mo, S. Zhu, T. Yao, J. Lian, A. M. Yacout, Journal of Nuclear Materials 495 (2017) 146–153.

[14] B. Beeler, M. Baskes, D. Andersson, M. W. Cooper, Y. Zhang, Journal of Nuclear Materials 495 (2017) 267–276.

[15] T. Yao, B. Gong, L. He, J. Harp, M. Tonks, J. Lian, Journal of Nuclear Materials (2017).

[16] Y. Miao, K. A. Gamble, D. Andersson, Z.-G. Mei, A. M. Yacout, Nuclear Engineering and Design 326 (2018) 371–382.

[17] G. L. Hofman, Journal of Nuclear Materials 140 (1986) 256–263.

[18] M. Finlay, G. Hofman, J. Snelgrove, Journal of nuclear materials 325 (2004) 118–128.

[19] A. Leenaers, S. Van den Berghe, E. Koonen, P. Jacquet, C. Jarousse, B. Guigon, A. Ballagny, L. Sannen, Journal of nuclear materials 327 (2004) 121–129.

[20] G. L. Hofman, Y. S. Kim, Nuclear Engineering and Technology 37 (2005) 299–308.

[21] Y. S. Kim, G. Hofman, J. Rest, A. Robinson, Journal of Nuclear Materials 389 (2009) 443–449.

[22] Y. S. Kim, Compr. Nucl. Mater. 3 (2012) 391.

[23] R. Birtcher, J. Richardson, M. Mueller, Journal of nuclear materials 230 (1996) 158–163.

[24] J. M. Harp, Personal communication, 2017. Idaho National Laboratory.

[25] R. Averback, R. Benedek, K. Merkle, Journal of Nuclear Materials 75 (1978) 162–166.

[26] C. Abromeit, Journal of nuclear materials 216 (1994) 78–96.

[27] M. Pellin, A. M. Yacout, K. Mo, J. Almer, S. Bhattacharya, W. Mohamed, D. Seidman, B. Ye, D. Yun, R. Xu, et al., Journal of Nuclear Materials 471 (2016) 266–271.

[28] B. Ye, L. Jamison, Y. Miao, S. Bhattacharya, G. Hofman, A. Yacout, Journal of Nuclear Materials 488 (2017) 134–142.

[29] S. Zinkle, L. Snead, Scripta Materialia (2017).

[30] J. F. Ziegler, M. D. Ziegler, J. P. Biersack, Nuclear Instruments and Methods in Physics Research Section B: Beam Interactions with Materials and Atoms 268 (2010) 1818–1823.

[31] R. E. Stoller, M. B. Toloczko, G. S. Was, A. G. Certain, S. Dwaraknath, F. A. Garner, Nuclear instruments and methods in physics research section B: beam interactions with materials and atoms 310 (2013) 75–80.

[32] B. Beeler, C. Deo, M. Baskes, M. Okuniewski, in: 2012 ANS Annual Meeting and Embedded Topical Meeting: Nuclear Fuels and Structural Materials for the Next Generation Nuclear Reactors, NFSM 2012; Chicago, IL; United States; 24 June 2012 through 28 June 2012;.

[33] Y. Miao, B. Beeler, C. Deo, M. I. Baskes, M. A. Okuniewski, J. F. Stubbins, Journal of Nuclear Materials 456 (2015) 1–6.

[34] D. Olander, Fundamental aspects of nuclear reactor fuel elements, 1976. URL: http://www.osti.gov/scitech/servlets/purl/7343826. doi:10.2172/7343826.

[35] J. Blanchard, D. Butt, M. Meyer, P. Xu, Development of Advanced High Uranium Density Fuels for Light Water Reactors, Technical Report Project No. 11-3041, U.S. Department of Energy Nuclear Energy University Programs (NEUP) Final Report, 2016.

[36] K. Remschnig, T. Le Bihan, H. Noël, P. Rogl, Journal of Solid State Chemistry 97 (1992) 391–399.

[37] K. Urso, K. Sridharan, B. Jaques, G. Alanko, D. Butt, M. Meyer, P. Xu, B. Tyburska-Päschel, Nuclear Technology 196 (2016) 100–110.

[38] K. Johnson, V. Ström, J. Wallenius, D. A. Lopes, Journal of Nuclear Science and Technology 54 (2017) 280–286.

[39] E. S. Wood, J. White, A. Nelson, Journal of Nuclear Materials 489 (2017) 84–90.

[40] E. S. Wood, J. T. White, A. T. Nelson, Journal of Nuclear Materials 484 (2017) 245–257.

[41] D. Kaletta, Radiation effects 78 (1983) 245–259.

[42] S. Kashibe, K. Une, K. Nogita, Journal of nuclear materials 206 (1993) 22–34.

[43] Q. Wei, N. Li, K. Sun, L. Wang, Scripta Materialia 63 (2010) 430–433.

[44] J. Rest, GRASS-SST: a comprehensive, mechanistic model for the prediction of fission-gas behavior in UO/sub 2/-base fuels during steady-state and transient conditions, Technical Report, Argonne National Lab., IL (USA), 1978.